Non-hydrostatic modelling of shallow water flow around a circular array of emergent cylinders

Jian Wang[1]
[1] School of Naval Architecture, Ocean and Civil Engineering, Shanghai Jiao Tong University, Shanghai 200240, China
abcr114@sjtu.edu.cn

Jingxin Zhang[1,2*]
[1] School of Naval Architecture, Ocean and Civil Engineering, Shanghai Jiao Tong University, Shanghai 200240, China
[2] MOE Key Laboratory of Hydrodynamics, Shanghai Jiao Tong University, Shanghai 200240, China
*Corresponding author: zhangjingxin@sjtu.edu.cn

Dongfang Liang[3]
[3] Department of Engineering, University of Cambridge, Cambridge CB2 1PZ, UK
dl359@cam.ac.uk

Lian Gan[4]
[4] Department of Engineering, Durham University, DH1 3LE, UK
lian.gan@durham.ac.uk

Abstract

This paper focuses on the investigation of the wake flow around a circular patch of cylinders with different solid volume fraction (SVF). The wake flow pattern was outlined by means of parameterizing the local water depth, the SVF and the flow stability factor *S*. The non-hydrostatic model was used to simulate the open channel flow through the cylinders. The turbulence was simulated using SST (shear strain transport) *k-ω* turbulence model. The model was firstly validated against experimental data to ensure the accuracy of the numerical simulation. Then the local turbulent flow and the wake flow field structures were investigated by changing the SVF and the water depth. The spatial evolution of the wake flow behind the patch was analyzed, and the correlation between the flow pattern and the wake flow stability was discussed. The cylinder-scale turbulence was intensive, even at low SVFs and low water depths. In contrast, the patch-scale turbulence in the wake was suppressed and the unsteady bubble wake was formed when the water depth decreasing, which revealed the effect of the bed friction force on the flow pattern. The parameter *S* and SVF were deduced to contribute to the formation of the different wake flow patterns.

Keywords: bed friction, shallow water flow, steady wake, vegetation flow, wake stability parameter

Introduction

Vegetation in fluvial systems plays a significant role in the sustainable development of aquatic systems because of its biological and hydrodynamic effects. It improves the water equality by the production of oxygen and uptake of nutrients. The biodiversity in rivers and oceans is promoted by providing food and creating different habitats. Also, by altering hydrodynamic conditions, such as flow velocity, turbulence structure and mass mixing, the exchanges of sediment, metals and other contaminants between terrestrial and aquatic systems can be well mediated. Aquatic plants can change the velocity field across different scales, ranging from individual branches and blades on a single plant to a patch of plants, called canopy or meadow (Nepf, 2012, Aberle &Järvelä, 2015). Generally, vegetation often exists in large-scale in coastal regions and rivers, and it forms a complex hydrodynamic environment (Yu *et al.*, 2014). The drag caused by large-scale vegetation in rivers can stabilize sediment and change the patterns of erosion and deposition. In nearshore regions, vegetation dissipates wave energy, which protects shoreline and riverbed from flood and wave attack. Therefore, it is of great significance to investigate the hydrodynamic influence of vegetation on shallow water flows (Wang *et al.*, 2018).

A variety of laboratory experiments on flow through vegetation were conducted over the last few decades. In these studies, the vegetation elements were usually

simplified as rigid bodies, and the vegetation zone was modelled by an array of solid cylinders (Zhan *et al.*, 2017, Poggi *et al.*, 2004, Nezu &Sanjou, 2008). Ball *et al.* (1996) measured the velocity vector fields associated with flow through pile groups in shallow water using particle tracking velocimetry (PTV). A steady low velocity near wake followed by an unstable far wake was observed downstream the structure. Chen and Jirka (1995) investigated the wake structure behind a porous plate further. Their observations show that the von Kármán vortex street originates at a distance downstream the porous obstruction. The region from the obstruction to the point where the vortex street forms is called the steady wake. Nicolle and Eames (2011) found that the vortex street did not appear at all for the SVF less than 0.05. Additionally, as the SVF decreases, the vortex street moves further downstream, resulting in a longer steady wake. In the experiments of Zong and Nepf (2012), the vortex development behind a patch of cylinders was studied, and a monotonous relationship between the dimensionless length of wake and the SVF was generalized.

Both small-scale and large-scale turbulence are generated when the open channel flow through a patch of cylinders. The small-scale turbulence is generated by the stem wake behind single cylinders, and the large-scale turbulence is produced in the wake behind the patch. Takemura and Tanaka (2007) investigated the flow structures and drag characteristics around a colony-type model, which comprises seven equally spaced emergent cylinders. They concluded that the change in the large-scale and small-scale vortex structures was related to the interaction between the water flow and the solid obstruction. The production of patch-scale turbulence is mainly caused by the separated shear layers (SSLs) form at the shoulders of the patch (Chang &Constantinescu, 2015). The patch-scale turbulence is often considered as horizontal two-dimension or quasi-two-dimension because of the low ratio of water depth to the patch scale. For shallow water flow, the turbulent flow is considered to be constrained by the rough bottom. Chu and Babarutsi (1988) concluded that the bed-friction generates not only the small-scale turbulence but, at the same time, exerts a stabilizing force on the large-scale turbulent coherent structures in shallow turbulent mixing layers. The vortex street behind a solid obstruction may be suppressed by the strong bed friction, which is characterized by a critical stability parameter, $S_c = 0.20$ (Ingram &Chu, 1987). Therefore, the development of patch-scale turbulence of the wake flow can also be impeded by the bed friction.

There is a periodic unsteadiness in the flow when the vortex shed off bluff bodies. It is one of the toughest tasks for turbulence modelling to accurately predict the unsteady turbulent flows (Xu &Ma, 2009, Wegner *et al.*, 2004, Durbin, 2002). Durbin (2002) argued that RANS cannot be applied to unsteady flow, unless there is a spectral gap between the unsteadiness and the turbulence. In the experiments of Zong and Nepf (2012), the vortex shedding frequencies were calculated to be around 2 Hz (cylinder-scale) and 0.1 Hz (patch-scale), and the gap between these shedding frequencies and the background turbulence was also observed. Thus, the RANS methods were still commonly used in practical simulations. Brito *et al.* (2016)

conducted the RANS simulations of compound open-channel flows with vegetated floodplains. Neary (2003) used a RANS-k-ω model to simulate flow through submerged vegetation. Yu *et al.* (2014) simulated flow through a circular patch of emergent cylinders using a horizontal two-dimensional multi-body model and porous model, respectively. Their achievements agreed well with the experimental data regarding the mean velocities, but failed to predict the magnitude of the turbulent fluctuation. Moreover, the influence of free surface and bed shear were not included in the 2D model. When the patch diameter D is much larger than the water depth H, the bed friction is large enough to suppress the vortex street and could not be ignored (Zong &Nepf, 2012). Under this condition, a robust 3D model should be considered.

In this paper, a 3D non-hydrostatic FVM model (HydroFlow®) based on unstructured grids is developed and used to simulate shallow water flow through a circular array of emergent cylinders. The flow patterns, turbulence intensity, and wake structures are analyzed in details preferring to different solid volume fractions and water depths.

Methods

Governing equations

In the present mathematical model, the total pressure is represented as a superposition of the hydrostatic component $p = \rho g\ (\eta - z)$ and the non-hydrostatic component q (Casulli &Stelling, 1998). The vertical coordinate z is transformed to the σ coordinate (Phillips, 1957) to fit the free surface and uneven bottom (see Figure 1). The modified equations are rewritten as:

$$\frac{\partial \eta}{\partial t}+\frac{\partial Hu}{\partial x}+\frac{\partial Hv}{\partial y}+\frac{\partial Hw_\sigma}{\partial \sigma}=0 \tag{1}$$

$$\frac{\partial Hu}{\partial t}+\frac{\partial Huu}{\partial x}+\frac{\partial Huv}{\partial y}+\frac{\partial Huw_\sigma}{\partial \sigma}=-gH\frac{\partial \eta}{\partial x}-\frac{H}{\rho}\frac{\partial q}{\partial x}+\frac{\partial}{\partial x}(\nu_t\frac{\partial Hu}{\partial x})+\frac{\partial}{\partial y}(\nu_t\frac{\partial Hu}{\partial y})+\frac{1}{H}\frac{\partial}{\partial \sigma}(\frac{\nu_t}{H}\frac{\partial Hu}{\partial \sigma}) \tag{2}$$

$$\frac{\partial Hv}{\partial t}+\frac{\partial Hvu}{\partial x}+\frac{\partial Hvv}{\partial y}+\frac{\partial Hvw_\sigma}{\partial \sigma}=-gH\frac{\partial \eta}{\partial y}-\frac{H}{\rho}\frac{\partial q}{\partial y}+\frac{\partial}{\partial x}(\nu_t\frac{\partial Hv}{\partial x})+\frac{\partial}{\partial y}(\nu_t\frac{\partial Hv}{\partial y})+\frac{1}{H}\frac{\partial}{\partial \sigma}(\frac{\nu_t}{H}\frac{\partial Hv}{\partial \sigma}) \tag{3}$$

$$\frac{\partial Hw}{\partial t}+\frac{\partial Hwu}{\partial x}+\frac{\partial Hwv}{\partial y}+\frac{\partial Hww_\sigma}{\partial \sigma}=-\frac{1}{\rho}\frac{\partial q}{\partial \sigma}+\frac{\partial}{\partial x}(\nu_t\frac{\partial Hw}{\partial x})+\frac{\partial}{\partial y}(\nu_t\frac{\partial Hw}{\partial y})+\frac{1}{H}\frac{\partial}{\partial \sigma}(\frac{\nu_t}{H}\frac{\partial Hw}{\partial \sigma}) \tag{4}$$

where η is the free surface elevation, h is the still water depth, and $H = h+\eta$ is the total water depth. u, v, w are the velocities in x, y, and z directions, respectively. $\sigma = (z-\eta)/(h+\eta)$ is the vertical coordinate in the computational domain. g is the gravitational acceleration. ν_t is the eddy viscosity coefficient. w_σ is the vertical velocity in σ coordinate, and can be derived from:

$$w_\sigma = \frac{w}{H} - \frac{u}{H}\left(\sigma\frac{\partial H}{\partial x} + \frac{\partial \eta}{\partial x}\right) - \frac{v}{H}\left(\sigma\frac{\partial H}{\partial y} + \frac{\partial \eta}{\partial y}\right) - \frac{1}{H}\left(\sigma\frac{\partial H}{\partial t} + \frac{\partial \eta}{\partial t}\right) \tag{5}$$

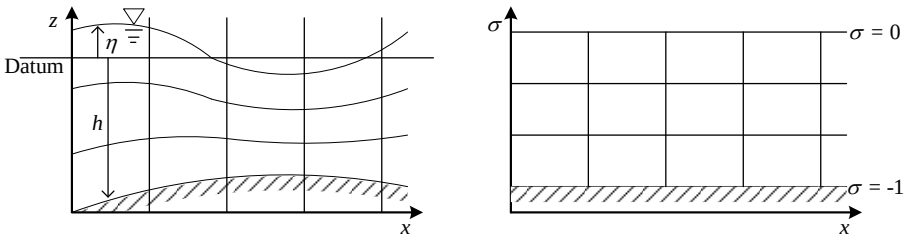

Figure 1 Sketch of transformed coordinates.

Turbulence model

The two-equation models have been widely adopted for turbulence closure in shallow water flows (Pu *et al.*, 2014, Pu, 2015). In the present study, the eddy viscosity coefficient ν_t is determined by the Shear-Stress Transport (SST) $k-\omega$ turbulence model (Menter, 1993). The transport equations for the turbulent kinetic energy k and the specific dissipation rate ω are as follows:

$$\frac{\partial(\rho k)}{\partial t} + \frac{\partial\left(\rho u_j k\right)}{\partial x_j} = \tau_{ij}\frac{\partial u_i}{\partial x_j} - \beta^*\rho\omega k + \frac{\partial}{\partial x_j}\left[\left(\mu + \sigma_k\mu_t\right)\frac{\partial k}{\partial x_j}\right] \tag{6}$$

$$\begin{aligned}\frac{\partial(\rho\omega)}{\partial t} + \frac{\partial\left(\rho u_j \omega\right)}{\partial x_j} &= \frac{\gamma}{\nu_t}\tau_{ij}\frac{\partial u_i}{\partial x_j} - \beta^*\rho\omega^2 + \frac{\partial}{\partial x_j}\left[\left(\mu + \sigma_\omega\mu_t\right)\frac{\partial \omega}{\partial x_j}\right] \\ &+2\rho\left(1-F_1\right)\sigma_{\omega 2}\frac{1}{\omega}\frac{\partial k}{\partial x_j}\frac{\partial \omega}{\partial x_j}\end{aligned} \tag{7}$$

the eddy viscosity coefficient ν_t is calculated as:

$$\nu_t = \frac{\mu_t}{\rho} = \frac{k}{\omega} \tag{8}$$

where ρ is the water density, μ is the dynamic viscosity and τ_{ij} is the Reynolds stress calculated as:

$$\tau_{ij} = \mu_t\left(\frac{\partial u_i}{\partial x_j} + \frac{\partial u_j}{\partial x_i}\right) - \frac{2}{3}\rho k\delta_{ij} \tag{9}$$

where δ_{ij} is the Kronecker delta. F_1 is a blending function, and the original sets of corresponding constants β^*, σ_k, γ, σ_ω and $\sigma_{\omega 2}$ are employed (Menter, 1993).

Numerical scheme

A two-step predictor-corrector scheme is used in the numerical method. The flow driven by the hydrostatic pressure is firstly calculated in the predictor step, and then the flow driven by the non-hydrostatic pressure is updated in the corrector step. In the numerical model, the grid system consists of unstructured meshes in the horizontal plane and multi-layers in the vertical direction. The governing equations are discretized based on the finite volume method (FVM). A 2nd order total variation

diminishing (TVD) scheme (OSHER scheme) is adopted to discretize the convective terms, and the central difference method is used to discretize the diffusion terms. In the corrector step, the Poisson-type equation for the non-hydrostatic pressure is numerically solved by a pre-conditioned BI-CGSTAB approach. The in-house codes (HydroFlow®) are paralleled by the OpenMP library (Zhang *et al.*, 2014).

Simulation implementation

Patch geometry

The same array geometry from experiments (Zong &Nepf, 2012) was chosen in the present work. Their measurements were conducted in a channel with a length of 13 m and a width of 1.2 m, which is shown in Figure 2. A circular patch of cylinders was put in the middle of the channel in a staggered arrangement. The leading edge of the patch was 3.0 m away from the inlet. The diameter d of a single cylinder was 0.6 cm, and the diameter D of the patch was 22 cm. The density of the cylinders within the patch was defined as the solid volume fraction (SVF), and was determined using $\varphi = n\pi d^2/4$, in which n (cm^{-2}) is the number of cylinders per unit horizontal area.

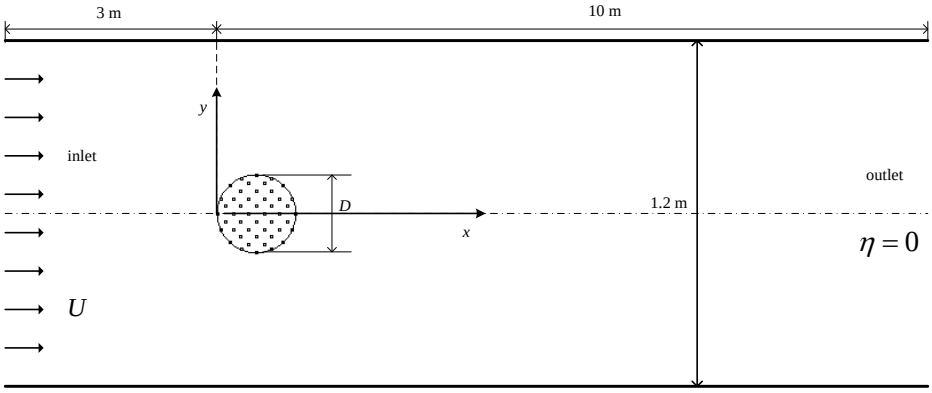

Figure 2 Definition sketch of the model.

Study cases and simulation implementation

A high grid resolution was designed in fitting the solid cylinder surface to meet the no slip solid wall boundary condition. A minimum normal scale of 0.1mm of the adjacent grids to the cylinder wall was chosen, which was about 2~5 dimensionless wall distance, i.e. Δ_n^+ = 2~5. On the bottom, the wall functions (10) were used to model the solid boundary, which require the first grids to the bottom lie in the fully developed turbulent boundary layer, i.e. $y^+ > 30$.

$$\frac{u}{u^*} = \frac{1}{\kappa}\ln\left(Ey^+\right) \qquad k = \frac{\left(u^*\right)^2}{\sqrt{C_\mu}} \qquad \omega = \sqrt{C_\mu}\,\frac{u^*}{\kappa y} \tag{10}$$

u^* is the friction velocity, C_μ is an empirical coefficient, and y^+ is the dimensionless length scale of the distance to the wall. Von Karman's constant κ = 0.41 and wall

roughness parameter $E = 9.8$.

A steady flow discharge was specified at the inlet of the numerical flume, and a steady water elevation was specified at the downstream outlet. The integration time step was 0.0005 s in all of the study cases. The simulations were firstly proceeded until the temporal water elevation probed at a fixed upstream observing point reached nearly steady, i.e. the calculated water elevation fluctuation decreased to ± 0.001 m. The computation was continually carried out during the next 60 s, meanwhile, the flow variables were recorded in a frequency of 20 Hz. The saved database was statistically analyzed to identify the wake flow patterns.

Case	φ	H (m)	Re_H	C_f	S	U_1/U	U_2/U	L_1/D
P1H1	0.10	0.03	2940	0.00720	0.053	0.16	1.24	4.06
P1H2	0.10	0.04	3920	0.00687	0.038	0.13	1.26	6.20
P1H3	0.10	0.0665	6517	0.00606	0.020	0.06	1.28	7.07
P1H4	0.10	0.10	9800	0.00551	0.012	0.08	1.23	4.81
P1H5	0.10	0.133	13034	0.00517	0.008	0.05	1.26	4.40
P1H6	0.10	0.200	19600	0.00473	0.005	0.07	1.28	4.45
P1H7	0.10	0.266	26068	0.00446	0.003	0.07	1.28	4.40
P2H3	0.03	0.0665	6517	0.00606	0.020	0.58	1.08	6.10
P2H5	0.03	0.133	13034	0.00517	0.008	0.57	1.08	9.03
P2H7	0.03	0.266	26068	0.00446	0.003	0.56	1.10	8.12

Table 1 Main geometrical and flow variables of the cases. The wake stability parameter is denoted by $S = C_f D/H$. The bed friction coefficient C_f was evaluated by the formula proposed by Silberman *et al.* (1963). U_1 is the mean streamwise velocity at the centreline of the steady wake, and U_2 is the velocity outside the wake. L_1 is the length of the steady wake, which was measured from the patch ($x/D = 1$) to the point where the velocity $\overline{u}$ began to increase.

$$\frac{1}{C_f} = -4\log\left(\frac{1.25}{4Re_H\sqrt{C_f}}\right) \tag{11}$$

Ten cases were numerically investigated in this study, with the solid volume fraction φ being 0.03 and 0.10, and the water depth H varying from 0.03 m to 0.266 m (see Table 1). $U = 0.098$ m/s was the free stream velocity at the inlet. The Reynolds number $Re_d = Ud/\nu$ was thus calculated to be 588.

Results and Discussion

Model validations

The simulated mean velocity profiles $\overline{u}$ (at $y = 0$) and $\overline{v}$ (at $y = D/2$) in the longitudinal direction were compared with experiments in Figure 3. To be consistent with the experiments of Zong and Nepf (2012), the velocity was measured at mid-depth. In Figure 3, the outer range of the cylinder patch is outlined from $x/D = 0$

to x/D = 1.0. In general, good agreements between the predicted and measured velocities were achieved, which validated the accuracy of the present model.

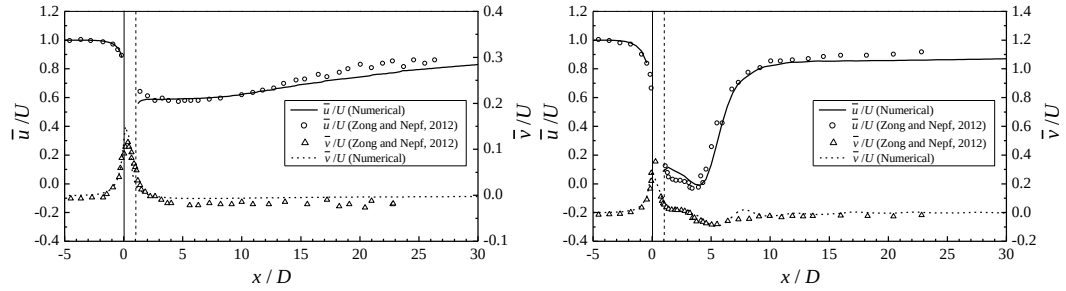

(a) P2H5 (b) P1H5

Figure 3 Longitudinal profiles of mean velocity $\overline{u}/U$ and $\overline{v}/U$ at $y = 0$.

Mean flow

Mean velocity

Flow around and through an array of cylinders exhibited a great difference to the flow around a solid body. At the centreline, the streamwise velocity decreased gradually from about 2D upstream of the patch. Within the patch, the streamwise velocity u decreased downstream because of the drag forces induced by cylinders. The mean velocity profiles (Figure 4a and Figure 5a) downstream a lower SVF patch (φ = 0.03) were nearly the same at different water depths. However, the spatial distributions of the mean streamwise velocity behind a dense patch (φ = 0.10) were distinct with the water depth varying. At large water depths (i.e. P1H5, P1H6, P1H7), there were only small discrepancies between the mean flow in the wakes. As shown in Figure 4b, the steady near wake extended further downstream and there was a longer distance for the wake velocity deficit recovery at small water depths. The recovery of the centreline velocity is known that the cross-wake mixing is mainly driven by the patch-scale vortex street. The analysis revealed that the patch-scale turbulence was weakened as H decreasing. The water depth was critical to the evolution of the wake flow; however, the length of the steady wake was found to be nonmonotonic with the water depth H. This was deduced that the change of wake structures was affected by the strong bed friction force. The flow reversal in the wake, which is indicative of a recirculation zone ($\overline{u} < 0$), was observed at large water depths and high SVF (Figure 4b). The recirculation zone moved downstream as H decreasing (i.e. P1H3, P1H4, P1H5), but it disappeared at very low water depths (i.e. P1H1, P1H2). Instead of changing the water depth, Zong and Nepf (2012) observed the same trend for the length of the recirculation zone by changing the SVF.

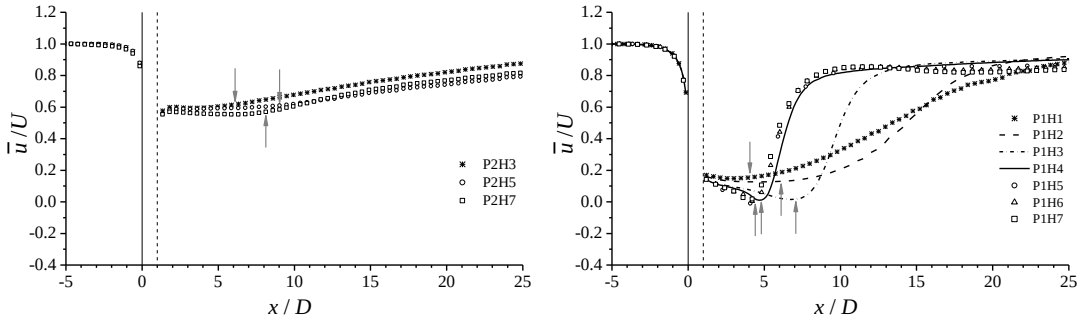

(a) φ = 0.03 (b) φ = 0.10

Figure 4 Longitudinal profiles of mean velocity $\overline{u}/U$ at centreline y = 0. The grey solid arrows locate the end of the steady wake of different cases. Since the length of the steady wake for P1H5, P1H6, and P1H7 has similar value, it is represented by the same arrow in Figure 4b.

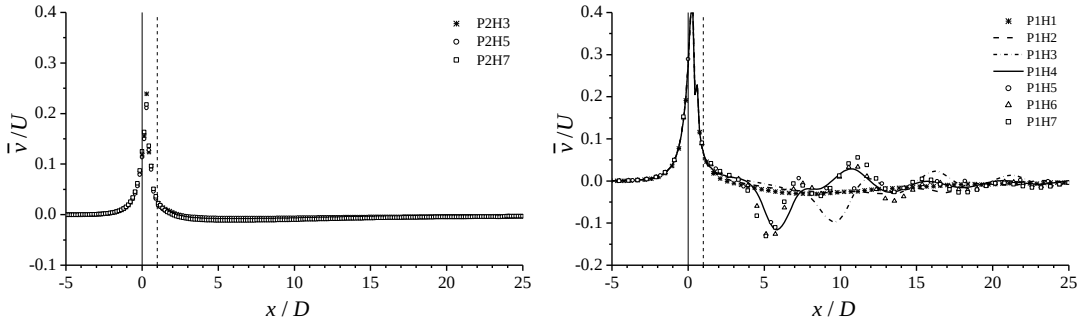

(a) φ = 0.03 (b) φ = 0.10

Figure 5 Longitudinal profiles of mean velocity $\overline{v}/U$ at $y = D/2$.

Turbulent kinetic energy

The influence of water depth on the turbulent structures was furtherly illustrated by the profiles of turbulent kinetic energy (TKE) (Figure 6). In the simulations, the TKE was comprised of two parts, i.e. TKE = k_{resolved} + k_{modelled}. The first constituent was obtained using the directly simulated velocity, which was calculated as $k_{\text{resolved}} = u_{rms}^2 + v_{rms}^2$. The other constituent was obtained from the turbulence Eqs (6) and (7), which was modelled by the turbulence model, i.e. $k_{\text{modelled}} = k$. For RANS-type model, the resolved TKE overwhelms the modelled TKE in the wake, i.e. $x/D > 1$ region, but the modelled TKE overwhelms the resolved TKE within the cylinder patch ($x/D < 1$) (Yu *et al.*, 2014). For convenience, the turbulent kinetic energy was normalized by the mean velocity and denoted as the turbulence intensity, $I_{\text{TKE}} = \sqrt{\text{TKE}}/U$.

In the wake of a patch, there were two distinct zones of elevated turbulence. The upstream peak of I_{TKE} (denoted as $I_{\text{TKE, }max}$) within the patch ($0 < x/D < 1$) indicated the small-scale turbulence generated by individual cylinders (Figure 6a). $I_{\text{TKE, }max}$ in Figure 6b appeared at a distance away from the patch ($x/D > 1$), which corresponded to the patch-scale turbulence. As shown in Figure 6, the variation of the small-scale

turbulence within the patch was relatively weak. That indicated the impact of bed friction on the cylinder-scale turbulence within the patch was negligible. To facilitate analysis, the cylinder-scale turbulence intensity at the end of the patch (x/D = 1) was characterized by *I*stem. Commonly, the turbulence intensity I_{TKE} in the sparse patch (φ = 0.03) was higher than that in the dense patch (φ = 0.1), which was because the wake-to-cylinder interactions were supressed at high SVF. For high SVF, the stem-scale turbulence was decayed rapidly through the patch. Behind the patch, the turbulence intensity decreased in the near wake, and then increased approaching to the downstream edge of the near wake. When the SSLs encountered, the turbulence intensity reached maximum and this peak contributed to the formation of large-scale Kármán vortex street (LKV). The profiles of I_{TKE} for large water depths (i.e. P1H5, P1H6 and P1H7) differed slightly. However, when *H* decreased under 0.133 m (i.e. P1H1, P1H2, P1H3 and P1H4), the position of the second $I_{TKE,\ max}$ moved further downstream, which indicated that the onset of patch-scale turbulence was delayed. The strength of the second $I_{TKE,\ max}$ decreased as *H* decreasing for both of SVFs. The simulations highlighted the turbulence intensity was weakened as *H* decreasing under one critical value, which resulted in a lower rate of the velocity recovery. Because the movement of SSLs contributed to the TKE behind the patch (Chang &Constantinescu, 2015), the spatial evolution of SSLs was suppressed by the bed friction, which was gradually distinguished when the water depth decreasing.

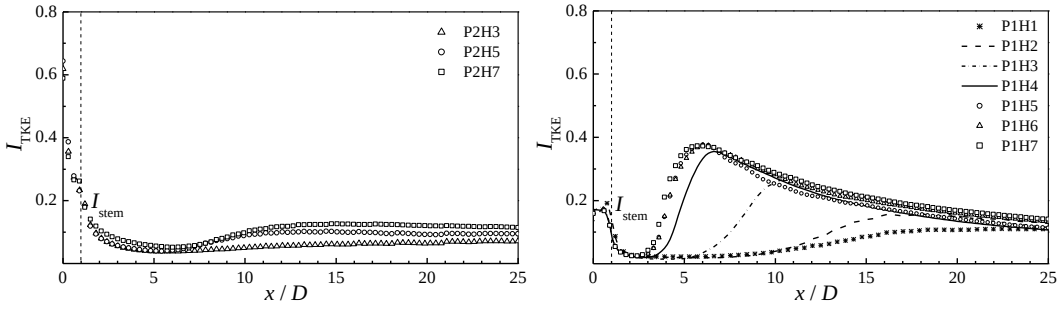

(a) φ = 0.03 (b) φ = 0.10

Figure 6 Longitudinal profiles of turbulent kinetic energy. The cylinder-scale turbulence intensity I_{stem} was evaluated at the end of the patch (x/D = 1).

Instantaneous vorticity filed

It is known that the time-averaged vorticity may smear out important information about the flow structures. Thus, the instantaneous vertical vorticity, ω_z was used to investigate the temporal and spatial evolution of the flow through the cylinder patch. When the upstream flow approached the cylinder patch, some water was forced around the patch and the residual water flowed through the patch. Because of the drag force on individual cylinders, there was a velocity deficit between the flow through the patch and the flow around the patch. Hence, two separated shear layers (SSLs) formed at each shoulder of the patch. These shear layers were separated by the flow through the patch (similar to a bleed flow) and extended a distance downstream the

patch until the LKV forming induced by the instability of the shear layer flow. For a high SVF and a large water depth (Figure 7a, b, c), the LKV behind the steady wake was clearly simulated. The LKV was also observed for a small water depth (Figure 7d, e), but the onset point was delayed compared with those cases shown in Figure 7a, b and c. When the water depth varying, the instantaneous vorticity revealed different spatial patterns. In Figure 7f and g, although the swirling vortices were visible, the vortex shedding process hardly occurred. This wake pattern was similar to the near wake behind a solid cylinder, which was labelled as unsteady bubble (UB) wake by Chen and Jirka (1995). The bed friction is much stronger as the water depth decreasing. The strong bed friction dissipated the flow energy and suppressed the spatial evolution of the separated shear layers originated at the patch shoulders. As a result, the formation of LKV was limited and the wake pattern changed. In contrast, the vorticity field for a sparse patch at different water depths did not change greatly. Since the patch-scale turbulence for a sparse patch was relatively weak, the vortex street was hardly genereated.

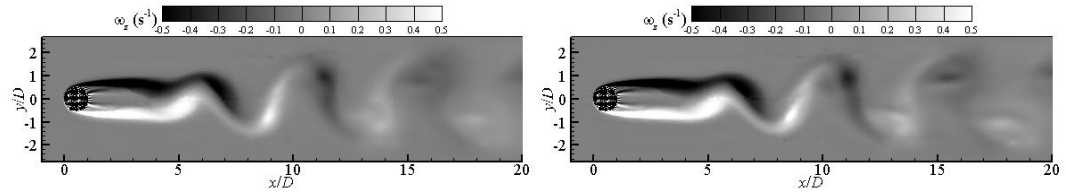

(a) P1H7 (b) P1H6

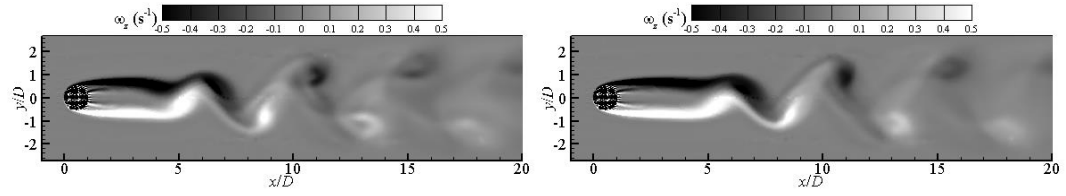

(c) P1H5 (d) P1H4

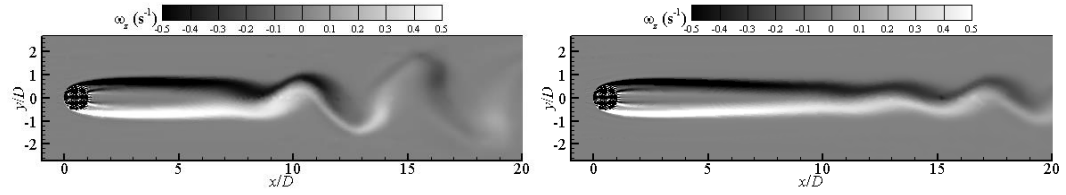

(e) P1H3 (f) P1H2

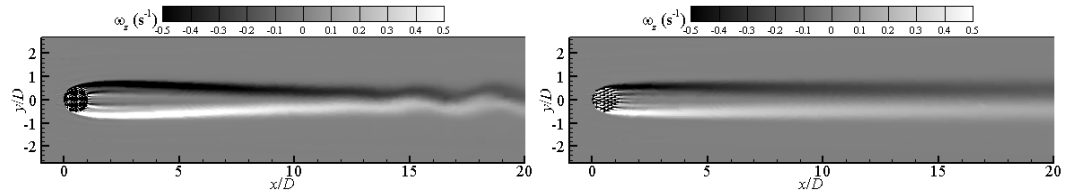

(g) P1H1 (h) P2H3

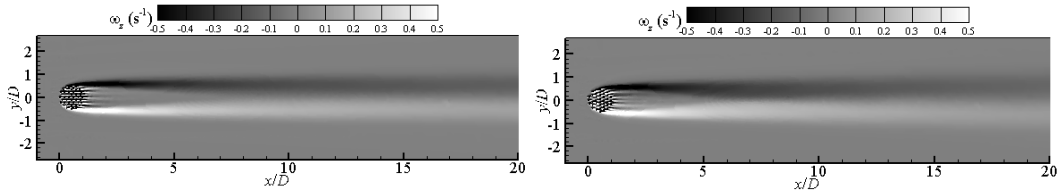

(i) P2H5 (j) P2H7

Figure 7 Contour map of instantaneous vertical vorticity.

Correlation of patch-scale turbulence with bed friction

To reveal the effect of the bed friction force on the patch-scale turbulence, the profiles of turbulence intensity in the vertical direction are displayed in Figure 8. In particular, the turbulent intensity was measured at the position where SSLs encountered (position of $I_{TKE,\ max}$ in Figure 6). Figure 8a shows the turbulence intensity at low SVF, in which the cases without cylinders are taken as comparisons. The maximum turbulence intensities of the cases with bare bed were found to be lower than the cylinder-scale turbulence intensities $I_{stem.}$ This explained that the turbulence within the cylinder array was dominated by wake generation, and it agreed with the observations of Nepf *et al.* (1997).

For low SVF, the bleed flow is strong, which weakens the formation and evolution of SSLs, and the turbulence intensity in the patch-scale wake is weak. Commonly, the turbulence intensity in the wake zone is weaker than cases with the bare bed. In free surface flows without lateral shear, the sizes of the turbulence structures are mainly governed by the balance of two forces. One force is the two-dimensional up-cascading of turbulent kinetic energy towards larger length scales at the free surface, and the other force comes from the interaction between large structures and the rough bottom (Uijttewaal &Tukker, 1998). Since the bed friction is the only force dominating the turbulence evolution in cases of bare bed, the turbulence intensities monotonously decrease from the near-bed region to the water surface. The curve for P2H3 in Figure 8a also exhibited this trend, and it can explain why the overall level of TKE in the patch-scale wake was lower than the other cases in Figure 6a. Because the bed shear effect is more and more strong as the water depth H decreasing, the turbulence intensity was gradually weaker (shown in Figure 8a and b).

By contrast, the turbulence intensity behind a dense patch was much stronger. The suppression of patch-scale turbulence was not distinctively observed until the water depth reduced under 0.04 m (see P1H2 in Figure 8b). As the turbulence generated by SSLs was highly suppressed by the bed friction at small water depths, the large-scale Kármán vortex street was gradually stabilized by the enhanced bed friction force. Additionally, the values of I_{TKE} measured at middle-depth z/H = 0.5 for cases P1H5, P1H6 and P1H7 were almost the same. The tiny differences between the results of these three cases were also observed in the mean flow and instantaneous vorticity field.

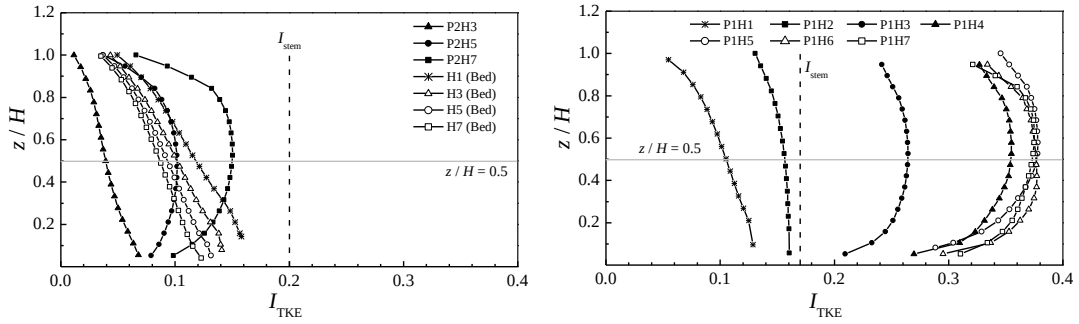

(a) φ = 0.03 (b) φ = 0.10

Figure 8 Profiles of turbulent kinetic energy in the vertical direction, measured at the position of I_{max} along centreline y = 0. The grey solid line z/H = 0.5 is the position of middle water depth, and the vertical dashed line represents the turbulence intensity at the end of the patch (x/D = 1), I_{stem}. The profiles of turbulence intensity without cylinders were plotted and labelled as "Bed".

The spatial evolution of the steady wake

In the steady wake of the cylinder patch, the SSLs were formed and enhanced downstream along the two sides of the wake region until they developed to the centreline of the wake region. Beyond the interaction position, the patch-scale vortex street formed. The length of the steady wake region, L_1, was therefore determined by the scale of the patch (D) and the growth rate of the SSLs. As shown in Figure 9, the characteristic width of the shear layer is δ, and a new width, δ_1, instead of δ, was used to calculate the growth rate of δ_1, i.e. dδ_1/dx.

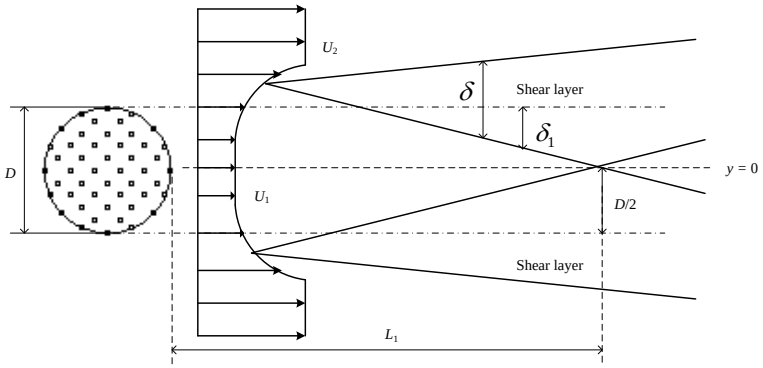

Figure 9 Sketch of the plane shear layer, and the definition of δ_1. U_1 is the low velocity within the steady wake, and U_2 is the velocity outside the wake.

δ_1 was defined as the distance from the shoulder of the array, i.e. y/D = 0.5, to the position where the mean velocity began to increase from U_1 to U_2. The values of δ_1 were obtained by measuring the lateral distribution of the mean streamwise velocity. Because of the porous obstruction blocking the flow, the velocity U_2 is always larger than the velocity U_1. The shear layer flows generated by the deficit between U_1 and U_2 developed laterally downstream until the two SSLs merged at the centreline of the wake zone. When the two SSLs merged at the centreline, the steady wake region was

closed and the width δ_1 reached maximum, i.e. $\delta_1 = D/2$. Beyond the steady wake region, the velocity at the centreline increased because of the strong exchange of the flow momentum. As a result of the interaction of SSLs, the flow speed recovered gradually to the upstream free-stream velocity U.

Figure 10 shows the dependence of $d\delta_1/dx$ on the stability parameter S. The shear layer growth rate for low SVF ($\varphi = 0.03$) was less than that for high SVF ($\varphi = 0.10$), which explained a longer steady wake region downstream a sparse cylinder patch. The shear layer growth rate decreased as S increasing, which indicated the transverse spreading rate of the shear layer decreased when the bed friction became the primary dynamic force on the turbulent flow (Chu &Babarutsi, 1988).

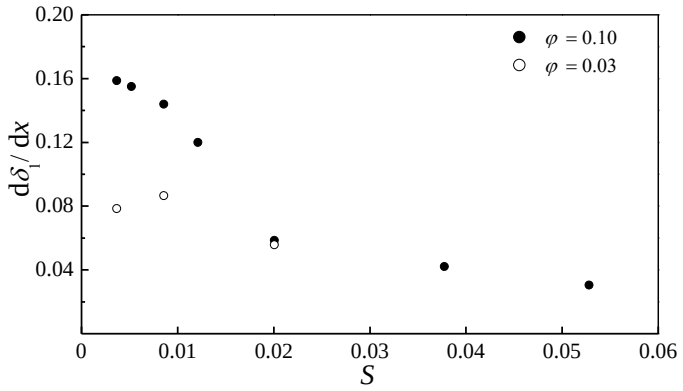

Figure 10 The growth rate of the shear layer against the parameter S.

The length of the steady wake was extensively measured. Drawing on the descriptions of planar shear layer growth (Champagne *et al.*, 1976) and assuming that the shear layer grows linearly, Zong and Nepf (2012) introduced a relationship to predict the length scale of the steady wake:

$$L_1 = \frac{D/2}{S_{\delta 1}} \frac{\bar{U}}{\Delta U} \tag{12}$$

where $\Delta U = U_2 - U_1$ is the velocity difference, $\bar{U} = (U_1 + U_2)/2$ is the averaged velocity. $S_{\delta 1}$ is an empirical parameter and was estimated as 0.10 in the experiments of Zong and Nepf (2012). Given the values of U_1 and U_2, the predicted dimensionless length scale L_1/D by Eq. (12) were plotted against the stability parameter S in Figure 11. As a comparison, the estimated L_1/D from the mean velocity profiles were also shown. The predicted results agreed well with simulated results when S was less than 0.02 regardless of the patch density. The relationship (12) failed to predict L_1 for both patches when S exceeds 0.02. One possible reason was that the parameter $S_{\delta 1}$ used by Zong and Nepf (2012) was constant and obtained from only one water depth, which was deduced to be critical to the bed friction force. Another reason was deduced that the assumption of the linear shear layer growth rate was invalid. Chu and Babarutsi (1988) also observed that the width of the mixing layer no longer increased linearly

with distance when the water depth was 2.5 cm. Particularly, the steady wake length L_1, reduced clearly as the bed friction force exceeded a critical value (e.g. $S > 0.03$ for $\varphi = 0.10$ and $S > 0.01$ for $\varphi = 0.03$). A conjectured explanation is the appearance of a recirculating bubble in the "UB" wake (see Figure 7). For a single cylinder, the wake is attached to the body, and the bubble length becomes stretched out as S growing (Chen &Jirka, 1995). Likewise, the reversal flow within the recirculating bubble pushed part of the fluid backward into the cylinder patch.

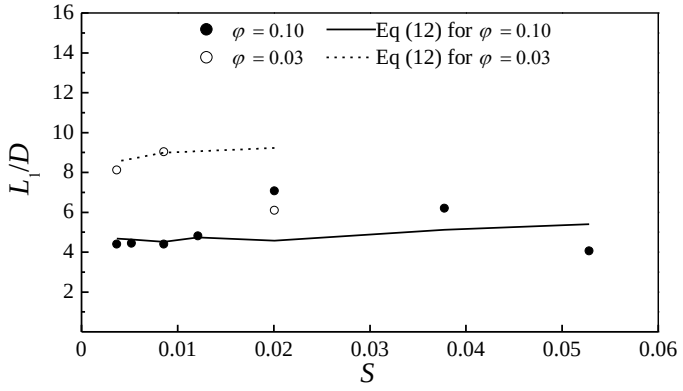

Figure 11 Dimensionless length of the steady wake, L_1/D.

Conclusions

In this paper, shallow water flows past a circular array of emergent cylinders have been numerically investigated. Ten study cases with different solid volume fractions of the patch and water depths were simulated, and the investigations focused on the correlations of the wake flow pattern with the SVF, water depth, bottom friction and the stability dynamic factor. The topic can help researchers investigate the influence of vegetation on patterns of deposition and erosion in shallow water flows.

The wake structure behind a circular array of cylinders was not only determined by the solid volume fraction, but also dependent on the bed friction. Two typical types of wake, the vortex street (VS) wake and the unsteady bubble (UB) wake were both observed in the simulations. For a solid cylinder, the VS-UB transition was characterized by a wake stability parameter, $S_c \approx 0.2$ (Chen &Jirka, 1995). However, Chen and Jirka (1995) also observed the unsteady bubble wake behind a porous plate for $S = 0.073$. This means that the critical wake stability parameter, S_c, for a porous patch maybe different from a solid body. Just in the scope of the present study cases, the critical S was preliminarily found to be 0.02 for $\varphi = 0.10$.

The bed friction played a different role in the cylinder-scale and patch-scale turbulent structures. Within the patch, even for the case of the sparse patch, the production of cylinder-scale turbulence was higher than the production by the bed shear. However, the patch-scale turbulence behind the patch can be greatly influenced by the bed friction. The peak of patch-scale turbulence occurred at the position where SSLs met and the shear layer instability took place. The von Kármán vortex street

may also form at this position, but it depended on the level of the patch-scale turbulence intensity. The VS was suppressed by the bed friction force, which happened when $S > 0.02$ for $\varphi = 0.10$.

The lateral growth of SSLs was slower when the bed friction increasing or the SVF decreasing. The length of the steady wake, L_1, was related to the growth rate of SSLs and the patch diameter D. Therefore, the L_1 obtained from the simulations were compared with an empirical relationship. It was noted that the empirical relationship failed to predict L_1 at $S > 0.03$ with $\varphi = 0.10$ and $S > 0.01$ with $\varphi = 0.03$. The assumption of linear shear layer growth and a constant empirical parameter $S_{\delta 1}$ possibly contributed to the failure of the empirical formula .

A critical parameter, S_c, was estimated to be 0.02 for high SVF ($\varphi = 0.10$), and the S_c decreased as φ decreasing. In order to extend a robust correlation between S_c and φ, a series of study cases with different SVFs must be supplemented and investigated.

Acknowledgements:

This work was sponsored by the National Nature Science Foundation (No. 11572196).

References

ABERLE, J. & J RVEL , J. 2015. Hydrodynamics of Vegetated Channels. *In:* ROWIŃSKI, P. & RADECKI-PAWLIK, A. (eds.) *Rivers – Physical, Fluvial and Environmental Processes.* Cham: Springer International Publishing.

BALL, D. J., ALLISON, N. & STANSBY, P. K. 1996. Modeling shallow water flow around pile groups. *Ice Proceedings Water Maritime & Energy,* 118**,** 226-236.

BRITO, M., FERNANDES, J. & LEAL, J. B. 2016. Porous media approach for RANS simulation of compound open-channel flows with submerged vegetated floodplains. *Environmental Fluid Mechanics,* 16**,** 1247-1266.

CASULLI, V. & STELLING, G. S. 1998. Numerical simulation of 3D quasi-hydrostatic, free-surface flows. *Journal of Hydraulic Engineering-Asce,* 124**,** 678-686.

CHAMPAGNE, F., PAO, Y. & WYGNANSKI, I. 1976. On the two-dimensional mixing region. *Journal of Fluid Mechanics,* 74**,** 209-250.

CHANG, K. & CONSTANTINESCU, G. 2015. Numerical investigation of flow and turbulence structure through and around a circular array of rigid cylinders. *Journal of Fluid Mechanics,* 776**,** 161-199.

CHEN, D. Y. & JIRKA, G. H. 1995. Experimental-Study of Plane Turbulent Wakes in a Shallow-Water Layer. *Fluid Dynamics Research,* 16**,** 11-41.

CHU, V. H. & BABARUTSI, S. 1988. Confinement and bed-friction effects in shallow turbulent mixing layers. *Journal of hydraulic engineering,* 114**,** 1257-1274.

DURBIN, P. A. 2002. A perspective on recent developments in RANS modeling. *Engineering*

Turbulence Modelling and Experiments 5, 3-16.

INGRAM, R. G. & CHU, V. H. 1987. Flow around Islands in Rupert Bay - an Investigation of the Bottom Friction Effect. *Journal of Geophysical Research-Oceans,* 92, 14521-14533.

MENTER, F. 1993. Zonal two equation kw turbulence models for aerodynamic flows. *23rd fluid dynamics, plasmadynamics, and lasers conference.*

NEARY, V. S. 2003. Numerical solution of fully developed flow with vegetative resistance. *Journal of Engineering Mechanics-Asce,* 129, 558-563.

NEPF, H., SULLIVAN, J. & ZAVISTOSKI, R. 1997. A model for diffusion within emergent vegetation. *Limnology and Oceanography,* 42, 1735-1745.

NEPF, H. M. 2012. Hydrodynamics of vegetated channels. *Journal of Hydraulic Research,* 50, 262-279.

NEZU, I. & SANJOU, M. 2008. Turburence structure and coherent motion in vegetated canopy open-channel flows. *Journal of Hydro-Environment Research,* 2, 62-90.

NICOLLE, A. & EAMES, I. 2011. Numerical study of flow through and around a circular array of cylinders. *Journal of Fluid Mechanics,* 679, 1-31.

PHILLIPS, N. A. 1957. A coordinate system having some special advantages for numerical forecasting. *Journal of Meteorology,* 14, 184-185.

POGGI, D., PORPORATO, A., RIDOLFI, L., ALBERTSON, J. D. & KATUL, G. G. 2004. The effect of vegetation density on canopy sub-layer turbulence. *Boundary-Layer Meteorology,* 111, 565-587.

PU, J. H. 2015. Turbulence modelling of shallow water flows using Kolmogorov approach. *Computers & Fluids,* 115, 66-74.

PU, J. H., SHAO, S. D. & HUANG, Y. F. 2014. Numerical and experimental turbulence studies on shallow open channel flows. *Journal of Hydro-Environment Research,* 8, 9-19.

SILBERMAN, E., CARTER, R., EINSTEIN, H., HINDS, J. & POWELL, R. 1963. Friction factors in open channels. *J Hydraul Div ASCE,* 89, 97-143.

TAKEMURA, T. & TANAKA, N. 2007. Flow structures and drag characteristics of a colony-type emergent roughness model mounted on a flat plate in uniform flow. *Fluid Dynamics Research,* 39, 694-710.

UIJTTEWAAL, W. & TUKKER, J. 1998. Development of quasi two-dimensional structures in a shallow free-surface mixing layer. *Experiments in Fluids,* 24, 192-200.

WANG, J., LI, L., ZHANG, J., LIANG, D. & YANG, Q. A 3D hydrodynamic model for shallow water flow through a circular patch of emergent cylinders. HIC 2018, 13th International Conference on Hydroinformatics, 1-6 July 2018 Palermo, Italy. EasyChair, 2268-2275.

WEGNER, B., MALTSEV, A., SCHNEIDER, C., SADIKI, A., DREIZLER, A. & JANICKA, J. 2004. Assessment of unsteady RANS in predicting swirl flow instability based on LES and experiments. *International Journal of Heat and Fluid Flow,* 25, 528-536.

XU, J. & MA, H. 2009. Applications of URANS on predicting unsteady turbulent separated flows. *Acta Mechanica Sinica,* 25, 319-324.

YU, L. H., ZHAN, J. M. & LI, Y. S. 2014. Numerical Simulation of Flow through Circular Array of Cylinders Using Multi-Body and Porous Models. *Coastal Engineering Journal,* 56.

ZHAN, J.-M., HU, W.-Q., CAI, W.-H., GONG, Y.-J. & LI, C.-W. 2017. Numerical simulation of

flow through circular array of cylinders using porous media approach with non-constant local inertial resistance coefficient. *Journal of Hydrodynamics, Ser. B,* 29**,** 168-171.

ZHANG, J. X., SUKHODOLOV, A. N. & HUA, L. 2014. Non-hydrostatic versus hydrostatic modelings of free surface flows. *Journal of Hydrodynamics,* 26**,** 512-522.

ZONG, L. J. & NEPF, H. 2012. Vortex development behind a finite porous obstruction in a channel. *Journal of Fluid Mechanics,* 691**,** 368-391.